

RSC Advances



This is an *Accepted Manuscript*, which has been through the Royal Society of Chemistry peer review process and has been accepted for publication.

Accepted Manuscripts are published online shortly after acceptance, before technical editing, formatting and proof reading. Using this free service, authors can make their results available to the community, in citable form, before we publish the edited article. This *Accepted Manuscript* will be replaced by the edited, formatted and paginated article as soon as this is available.

You can find more information about *Accepted Manuscripts* in the [Information for Authors](#).

Please note that technical editing may introduce minor changes to the text and/or graphics, which may alter content. The journal's standard [Terms & Conditions](#) and the [Ethical guidelines](#) still apply. In no event shall the Royal Society of Chemistry be held responsible for any errors or omissions in this *Accepted Manuscript* or any consequences arising from the use of any information it contains.

ARTICLE

Non-invasive imaging of breast cancer using RGDyK functionalized fluorescent carbonaceous nanospheres

Cite this: DOI: 10.1039/x0xx00000x

Shaobo Ruan^{a,1}, Jun Qian^{b,1}, Shun Shen^b, Jiantao Chen^a, Xingli Cun^a, Jianhua Zhu^b, Xinguo Jiang^b, Qin He^{a,*} and Huile Gao^{a,*}

Received 00th January 2012,
Accepted 00th January 2012

DOI: 10.1039/x0xx00000x

www.rsc.org/

Fluorescent carbonaceous dots (CDs) have attracted much attention due to their unique properties. However, their application in non-invasive imaging of diseased tissues was restricted by the short excitation/emission wavelength and the poor targeting efficiency of CDs. In this study, CDs were prepared from sucrose and glutamic acid with a particle size of 57.5 nm. Obvious emission could be observed at 600 nm to 700 nm when excited at around 500 nm. This property enabled CDs with capacity for deep tissue imaging with low background adsorption. RGD, a ligand which could target to most tumor and neovasculature cells, was anchored onto CDs after PEGylation. The product, RGD-PEG-CDs could accumulate in MCF-7/ADR xenografts at high intensity, which was 1.65-fold higher than that of PEG-CDs. Furthermore, RGD-PEG-CDs showed well colocalization with neovasculature. Thus, RGD-PEG-CDs could be used for non-invasive MCF-7/ADR tumor imaging.

CDs functionalized with other ligands may also be used as a non-invasive probe for many kinds of tumor imaging.

Introduction

Fluorescent probes have been widely used for particle tracking and labelling, virus labelling, and small compounds tracking^{1,2}. Among the probes, fluorescent carbonaceous dots (CDs) have gained extensive attention due to not only their unique characteristics, such as green synthetic route, optical stability, well compatibility and low toxicity, but also their great potential for application in detection and catalysis³⁻⁶. To obtain CDs, many methods were developed, including thermal/hydrothermal oxidation, electrochemical synthesis and microwave/ultrasonic synthesis⁴. Among which, one-step hydrothermal/thermal treatment methods have been widely used in producing CDs from various biomaterials, such as silk, juice, glucose, or other synthetic polymers⁷⁻⁹. However, Most of these produced CDs showed short excitation/emission wavelength (lower than 500 nm for excitation wavelength and 600 nm for emission wavelength), which restricted the application in bio-imaging of diseases such as tumor, especially in the non-invasive whole body imaging, owing to the high background adsorption^{10,11}. Thus preparing CDs with near-infrared (NIR) fluorescence spectrum is critical for expanding the application of CDs to non-invasive whole-body imaging. Unfortunately, few CDs displayed strong emission intensity when changed the excitation wavelength from blue or green to red or NIR region and no studies have reported non-invasive whole body imaging of diseased tissue using these CDs^{3,12-14}. Besides the property of CDs, the physical barrier of the diseased tissue is another obstacle that restricted the application

in non-invasive imaging, and rear studies have used CDs in biological imaging^{15,16}. Tumor is one of the biggest threats for human being. Multidrug resistance further restricted distribution of drugs or probes in the tumor cells, resulting poor tumor treatment outcome and low tumor/normal tissue ratio^{17,18}. Nanoparticulated systems could passive target to these tumors utilizing enhanced permeability and retention (EPR) effect¹⁹⁻²³. Surface modification of these systems with tumor homing ligands could further improve the accumulation in tumor site and the internalization by tumor/tumor associated cells, leading to better drug delivery efficiency and higher imaging ability²⁴⁻²⁷. Integrin, such as $\alpha_v\beta_3$, is overexpressed on many kinds of tumor cells and tumor neovascular cells^{28,29}. The corresponding ligand, RGD, was widely used as a specific ligand to improve the tumor and neovasculature targeting efficiency of nanoparticulated systems³⁰⁻³². Thus, RGD was selected to be anchored CDs for non-invasive cancer imaging. In this study, a new method was developed to produce CDs with relatively long excitation/emission wavelength. The characteristics of the CDs were evaluated by several experiments. To evaluate the targeting efficiency of RGD modified CDs (RGD-PEG-CDs), a kind of multidrug resistance breast cancer cell line, MCF-7/ADR, was used in this study.

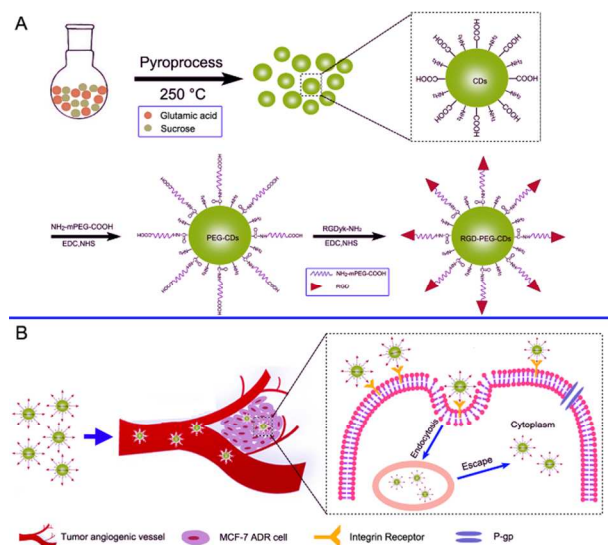


Figure 1. A: Elucidation of the preparation procedure of RGD-PEG-CDs. B: Elucidation of transportation and uptake procedure of RGD-PEG-CDs.

Materials and methods

Materials

RGDyK-NH₂ was synthesized by GL Biochem Co., Ltd. (Shanghai, China). PEG-NH₂ (Mw=5000) and HOOC-PEG-NH₂ (Mw=5000) were purchased from Seebio (Shanghai, China). Glutamic acid and sucrose were purchased from Sinopharm Chemical Reagent (Shanghai, China). MCF-7/ADR cell line was kindly provided by Prof. Lu, Beijing University. Dulbecco's Modified Eagle Medium (high glucose) cell culture medium (DMEM) and FBS were purchased from Life Technologies (NY, USA). Cell culturing dishes and plates were purchased from Cyagen Biosciences Inc. (Guangzhou, China). N-(3-dimethylaminopropyl)-N'-ethylcarbodiimide hydrochloride (EDC) and N-hydroxy-succinimide (NHS) were purchased from Sigma (MO, USA). DAPI was purchased from Beyotime (Haimen, China). Rabbit anti-CD31 antibody was purchased from Abcam (Hong Kong, China). Alexafluor 594-conjugated donkey anti rabbit antibody was purchased from Jackson ImmunoResearch Laboratories, Inc. (PA, USA). LysoTracker red was purchased from Life Technologies (NY, USA). HUVEC was purchased from the Institute of Biochemistry and Cell Biology, Shanghai Institutes for Biological Sciences, Chinese Academy of Sciences (Shanghai, China). MCF-7/ADR cells were kindly donated from school of Pharmacy, Peking University (China). BALB/c nude mice (male, 4-5 weeks, 18-22 g) were obtained from the Animal Research Center of Sichuan University (Chengdu, China) and maintained under standard housing conditions. All animal experiments were carried out in accordance with protocols evaluated and approved by the ethics committee of Sichuan University.

Preparation and characterization of RGD-PEG-CDs

As shown in Figure 1, a dry flask (100 mL) was heated to 250 °C, and then 1 g of glucose was added. One minute later, 0.1 g of glutamic acid was added and the heater was removed. When the temperature of the flask decreased to approximately 50 °C,

5 mL of deionized water was added to suspend the produced CDs.

To prepare PEGylated CDs (PEG-CDs), CDs were activated by EDC/NHS for 0.5 h, followed with the adding of PEG-NH₂. After 6 h incubation, the PEG-CDs could be obtained after dialysis (MW=10000D). To prepare RGD-PEG-CDs, CDs were firstly reacted with HOOC-PEG-NH₂ then the production was further activated by EDC/NHS and RGDyK-NH₂ was added into the solution. Another 6 h later, the RGD-PEG-CDs could be obtained after dialysis (MW=10000D).

The particle size and morphology were observed through transmission electron microscope (H-600, Hitachi, Japan). The hydrated particle size and zeta potential were determined by a zeta/particle sizer (Malvern, NanoZS, Germany). To determine the surface density of PEG, the unconjugated PEG was removed by dialysis and recovered by freeze-drying. Then the unconjugated PEG was dissolved and determined by barium chloride method. Briefly, 0.6 mL of PEG contained solution was added with 1.2 mL of 5% barium chloride. After reaction, 60 μL of 0.025 mol/L I₂ was added and absorbance at 385 nm was determined. The surface density of RGD was further determined, the unconjugated RGD was removed by dialysis and recovered by freeze-drying. Then the unconjugated RGD was dissolved and determined by BCA method. Briefly, 0.1 mL of RGD contained solution was added with 2 mL of BCA working reagent. The solution was incubated at 60°C for 30 min and determined at 562 nm. Fluorescence spectrum was evaluated using a RF-5301PC spectrofluorophotometer (Shimadzu, Japan). X-ray photoelectron spectroscopy (XPS) experiments were performed on an AXIS Ultra DLD (Kratos UK) with Mg Ka radiation (hν = 1486.6 eV), with a chamber pressure of 2.2×10⁻⁹ Torr. The source power and high voltage was set at 150W and 15kV, and pass energies of 40 eV for survey scans was used. The analysis spot size was 300×700 μm. The data was analyzed by PHI-MATLAB software with C1s = 284.6 eV as a benchmark for the binding energy correction. Fluorescence quantum yields were evaluated using a RF-5301PC spectrofluorophotometer (Shimadzu, Japan).

Serum stability and safety

The stability of CDs was evaluated in PBS with different concentrations of FBS. CDs, PEG-CDs and RGD-PEG-CDs were suspended in 0%, 10% or 50% FBS and incubated in a 37 °C incubator. The absorption at 560 nm was determined by a microplate reader (Multiskan MK3, Thermo, USA) at 0, 1, 2, 3, 4, 6, 8, 12 and 24 h.

To evaluate the hemocompatibility, whole blood was collected from mice using heparin as anticoagulant. After centrifugation at 1500 rpm for 5 min, the red blood cells were resuspended in PBS at the final density of 2%. Different concentrations of CDs, PEG-CDs and RGD-PEG-CDs were added into cell suspension and incubated at 37 °C for different periods of time³³. After incubation, cell suspension was centrifuged at 1500 rpm for 5 min, and the adsorption of supernatant at 560 nm was determined by a microplate reader (Thermo Scientific Varioskan Flash, USA). 1% of Triton X-100 was used as positive control and PBS was used as negative control.

The cytotoxicity of different formulations was evaluated by MTT assay. HUVEC cells and MCF-7/ADR cells (2×10⁴ cells/mL) were seeded in 96-well plates. Twenty-four hours later, CDs, PEG-CDs and RGD-PEG-CDs were added into wells with a serial concentrations ranging from 5 mg/mL to 1 μg/mL. Twenty-four hours later, 100 μL of MTT solution was added into each well and incubated for 4 h. After replacing the

medium with DMSO, the 490 nm absorption was observed by a microplate reader (Thermo Scientific Varioskan Flash, USA).

In vitro cellular uptake and subcellular localization

MCF-7/ADR cells were seeded in 6-cm glass-bottom dishes at a density of 1×10^4 cells/mL and incubated at 37 °C for 24 h. After 5-min incubation in PBS, the cells were treated with different concentrations of PEG-CDs and RGD-PEG-CDs for different times. After incubation, the cells were washed, fixed and stained with 0.5 µg/mL of DAPI. Images were captured with a confocal microscope (LSM710, Carl Zeiss, Germany).

To determine the subcellular colocalization with endosomes, MCF-7/ADR cells were seeded into dishes as described above and incubated with 125 µg/mL of PEG-CDs or RGD-PEG-CDs for 0.25 h or 4 h. Thirty minutes before the incubation ended, LysoTracker Red (100 nmol/L) was added into the wells. After incubation, the cells were washed, fixed and stained with 0.5 µg/mL of DAPI. Images were captured with a confocal microscope (LSM710, Carl Zeiss, Germany).

Uptake mechanism

MCF-7/ADR cells were seeded in 12-well plates at a density of 5×10^4 cells/mL and incubated for 24 h. After a 20-min pre-incubation in DMEM, the cells were treated with 125 µg/mL of PEG-CDs or RGD-PEG-CDs at the presence of various inhibitors for 1 h at 37 °C, respectively: PBS (control), 20 µg/mL chlorpromazine, 10 µg/mL filipin, 0.1% w/v sodium azide, 20 µg/mL nocodazole, 25 µg/mL colchicine, 400 µg/mL poly-L-lysine and 200 µg/mL RGDyK. Cells incubated with PEG-CDs or RGD-PEG-CDs at 4 °C were also used to determine the uptake mechanism. After washing with ice-cold PBS 3 times, the cells were digested and the mean fluorescence intensity was observed by flow cytometry (FACS Aria Cell Sorter, BD, USA).

In vivo and ex vivo imaging and slice distribution

The MCF-7/ADR xenografts bearing mice were established through injecting of 1×10^7 MCF-7/ADR cells into the right flank of the mice as described previously³⁴. The length and width of the tumor were determined every two days using a caliper, and the volume was calculated using following equation: tumor volume = (length × width²)/2. After the volume of the tumor was approximately 100 mm³, mice were i.v. administered 50 mg/kg of PEG-CDs or RGD-PEG-CDs through tail vein. Then the whole body fluorescent distribution was observed through an *in vivo* imaging system (IVIS Spectrum, Caliper, USA) 5, 15, 30, 60, 120, 180 and 240 min after injection. Then, the mice were sacrificed, and their tissues were subjected to *ex vivo* fluorescence imaging. After fixed with 4% paraformaldehyde, organs were further dehydrated by 15% sucrose followed with 30% sucrose. Consecutive frozen sections of 10 µm thicknesses were prepared and then stained by 0.5 µg/mL DAPI for 5 min. For tumor slices, microvessel was stained with rabbit anti-CD31 antibody (1:200) followed with Alexafluor 594 conjugated donkey anti rabbit antibody according to previous established procedure³⁵. The distribution of fluorescence was observed by a confocal microscope (LSM710, Carl Zeiss, Germany).

Statistical analysis

Data were presented as mean ± SD. Statistical differences in the experiments were determined by the student *t* test.

Results and discussion

Characterization of RGD-PEG-CDs

CDs were prepared from sucrose and glutamic acid through thermal treatment. The hydrated particle size of CDs was 57.5 nm with a polydispersity index of 0.147 (Figure 2A), while the zeta potential was -23.5 mV. According to transmission electron microscope (TEM) (Figure 2D), the particles were well dispersed with spherical shape. There were plenty of carboxyl group on surface of CDs¹⁶, which could be used for PEGylation and other modification. After modification with PEG and RGD, the density of PEG and RGD was 4.04 ± 0.02 µg/mg CDs and 1.91 ± 0.02 µg/mg CDs respectively. The hydrated particle sizes of PEG-CDs and RGD-PEG-CDs were changed to 63.2 nm and 67.4 nm (Figures 2B and C. Table 1). The elevation in particle sizes was contributed by the surface modification. However, the zeta potential was not considerably changed.

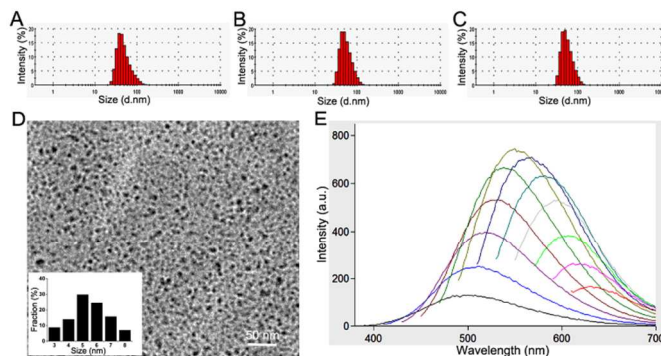


Figure 2. DLS data of CDs (A), PEG-CDs (B) and RGD-PEG-CDs (C). D: TEM image of CDs, bar represents 50 nm, inner picture was semi-quantitative data of TEM image. E: Fluorescent spectrum of CDs at excitation wavelength from 340 nm to 560 nm.

Table 1. Particle size and zeta potential of PEG-CDs and An-PEG-CDs. (n=3)

Formulations	Particle size (nm)	PDI	Zeta potential (mV)
CDs	57.5±1.4	0.147±0.078	-23.5±2.7
PEG-CDs	63.2±3.1	0.181±0.105	-20.3±1.1
RGD-PEG-CDs	67.4±4.6	0.197±0.028	-22.8±1.5

The highest absorbance of CDs was 340 nm according to UV-vis spectrum (Supporting Figure S1). Interestingly, when we increased the excitation wavelength of the CDs from 340 nm to 440 nm, both the emission wavelengths and fluorescent intensity increased (Figure 2E), which was significantly different from previous reported CDs^{9,36}. The highest emission wavelength was 552 nm while the excitation wavelength was 440 nm, which was longer than recently reported CDs possessing highest excitation/emission wavelength of 420 nm and 520 nm¹². Additionally, further increasing the excitation wavelength could also expand the emission wavelength, displaying a broad excitation and emission range. Although the intensity peak of emission decreased with increasing of

excitation wavelengths from 440 nm to 560 nm, there were still apparently emission peaks. The fluorescent property of the CDs was useful for *in vivo* imaging because longer excitation/emission wavelength could endow the CDs with the ability to penetrate deeper tissues. The quantum yields of CDs and RGD-PEG-CDs were 37.5% and 21.7% respectively, which were higher than many other reports^{15, 37}.

Surface state of CDs was further characterized by XPS. The XPS overall spectrum showed three main peaks at 284.6, 399.7, 531.7 eV (Supporting Figure S2A), contributed to the C_{1s}, N_{1s}, O_{1s} respectively. The C_{1s} spectrum (Supporting Figure S2B) displayed four peaks at 284.60, 285.11, 286.06, 288.31 eV, which were attributed to C-C, C-N, C-O and C=N/C=O groups, respectively^{16, 38}. The N_{1s} spectrum (Supporting Figure S2C) displayed three peaks at 399.05, 399.81 and 400.85 eV, which were attributed to C-N-C, C-N and N-H groups, respectively³⁹. The O_{1s} spectrum (Supporting Figure S2D) exhibited two peaks at 531.56 and 532.80 eV, which were owing to C=O and C-OH/C-O-C groups, respectively¹⁶. These results demonstrated that the surface of CDs possessed plentiful oxygen and nitrogen functional groups, which was consistent with previous studies and useful for further modification. Similar peaks were observed in the spectrum of PEG-CDs (Supporting Figure S2E, F, G and H). The concentration of C in the surface of PEG-CDs was higher than that of CDs, contributing to the higher C concentration in PEG, suggesting the PEG was successfully anchored onto CDs. Furthermore, the spectrum of RGD-PEG-CDs also showed the similar peaks (Supporting Figure S2I, J, K and L). The concentration of C and O in the surface RGD-PEG-CDs was close to that of PEG-CDs, while the concentration of N was relatively higher than that of PEG-CDs, indicating that the RGD was successfully conjugated onto PEG-CDs. Until recently, the actual photoluminescence mechanism of CDs remained unclear. It supposed that the surface-defect based mechanism might contribute to the luminescence of CDs⁷. In this study, amine groups were doped in the surface of CDs, which may also contribute to the luminescence of CDs³⁶.

Evaluation of CD serum stability, hemocompatibility and cytotoxicity

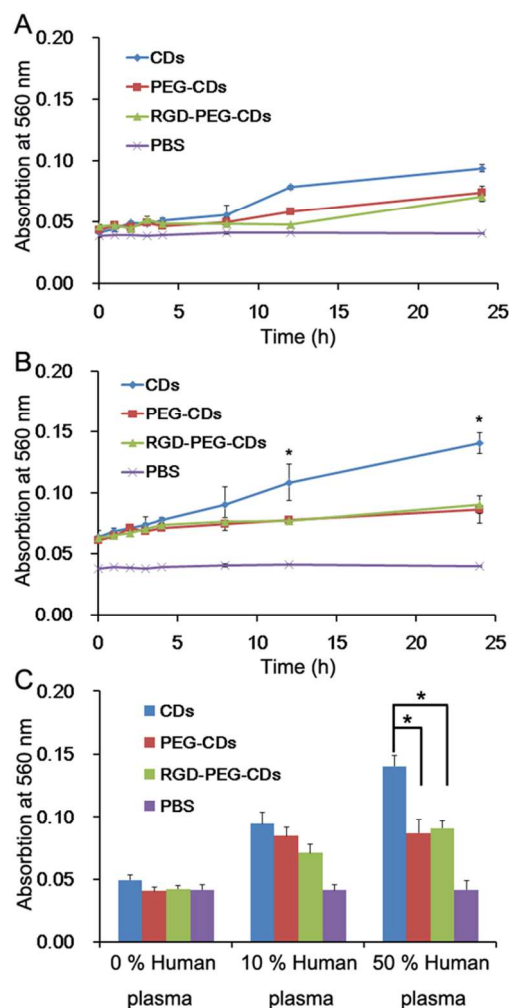


Figure 3. Serum stability of CDs, PEG-CDs and RGD-PEG-CDs in serum. A: Time related absorption of 100 $\mu\text{g}/\text{mL}$ of CDs, PEG-CDs and RGD-PEG-CDs after incubation with 50% FBS. B: Absorption of 100 $\mu\text{g}/\text{mL}$ of CDs, PEG-CDs and RGD-PEG-CDs after 24 h incubation with different concentrations of FBS. * $p < 0.05$.

In order to be used in bio-systems, the particles should be stable in the blood circulation. Thus serum stability was evaluated by incubation with different concentrations of serum for different periods of time. The adsorption of protein onto particles could increase the turbidity leading to the elevating of absorption at 560 nm (Figure 3). The absorption of CDs at 560 nm significantly increased during the increase of incubation time, suggesting the CDs could considerably adsorb serum protein at a time-dependent manner. Comparatively, after PEGylation, the absorption of both PEG-CDs and RGD-CDs were significantly lower than that of CDs, demonstrating the PEGylation could inhibit the protein adsorption and increase the serum stability⁴⁰. Incubation of CDs, PEG-CDs and RGD-PEG-CDs with different concentrations of serum also demonstrated CDs could adsorb significantly more proteins than the amount adsorbed by PEG-CDs and RGD-PEG-CDs (Figure 3B).

Hemocompatibility was carried out using fresh 2% blood red cells. Although the hemolysis rate increased over time, the rates of PEG-CDs and RGD-PEG-CDs were significantly lower than that of CDs (Figure 4A). For example, at the concentration of 5 mg/mL, the hemolysis rate of CDs was 21.1% after 12 h incubation (Figure 4B). However, the rates of PEG-CDs and RGD-PEG-CDs were only 13.6% and 14.6% respectively,

which were similar to that of PBS. The images of blood cells after 8 h incubation also demonstrated the lower hemolysis rate of PEG-CDs and RGD-PEG-CDs compared to CDs (Figure 4C). These results indicated the PEGylation could improve the compatibility, which was consistent with previous results¹⁶.

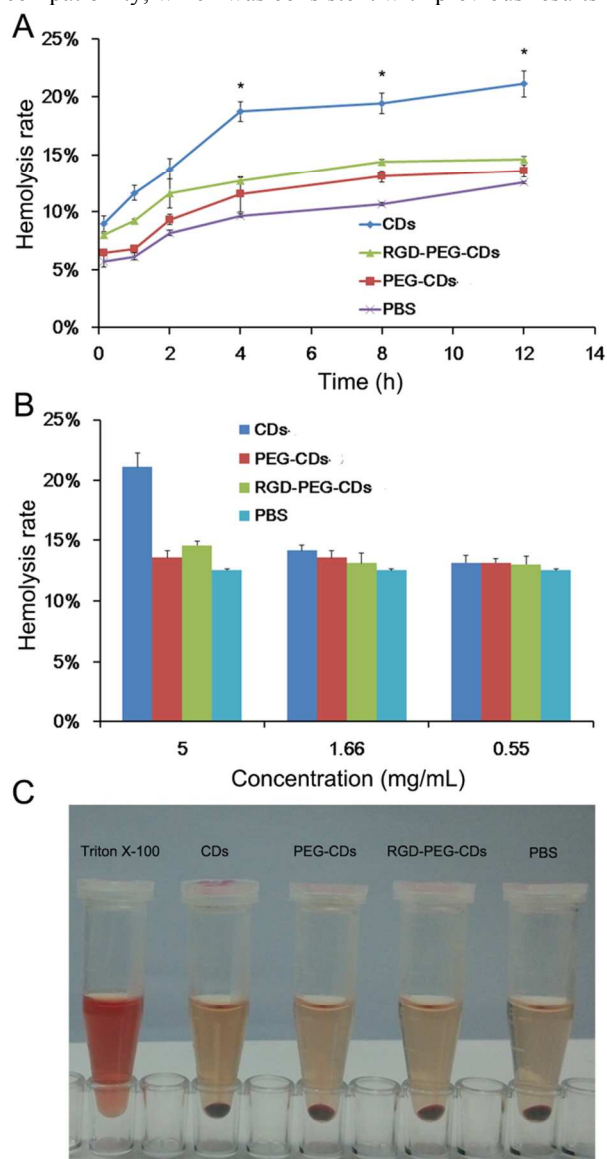


Figure 4. Hemocompatibility of CDs, PEG-CDs and RGD-PEG-CDs. A: Time-related hemolysis rates of 5 mg/mL of CDs, PEG-CDs and RGD-PEG-CDs. * $p < 0.05$ vs PEG-CDs and RGD-PEG-CDs. B: Concentration related hemolysis rates of different concentrations of CDs, PEG-CDs and RGD-PEG-CDs incubated with red blood cells for 8 h. C: Image of red blood cells incubated with 5 mg/mL of CDs, PEG-CDs and RGD-PEG-CDs for 8 h.

MTT assay was performed on both HUVEC and MCF-7/ADR cells. The cell viabilities of both MCF-7/ADR cells and HUVEC did not significantly decrease after 24 h incubation with CDs, PEG-CDs or An-PEG-CDs at concentrations lower than 1 mg/mL (Figure 5). Thus it could be concluded that CDs displayed low toxicity, which was consistent with previous reports¹¹.

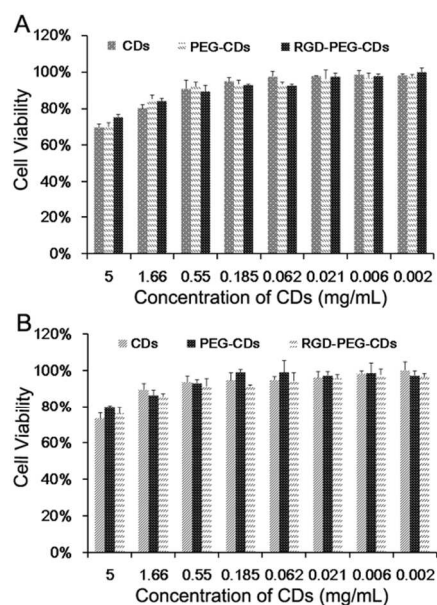


Figure 5. MTT assay of different concentrations of CDs, PEG-CDs and RGD-PEG-CDs on MCF-7/ADR cells (A) and HUVEC cells (B).

Cellular uptake

To determine their potential application in tumor imaging, *in vitro* cellular uptake was carried out. The fluorescent intensity of cells increased when elevating the concentration of PEG-CDs or expanding the incubation time, suggesting the uptake of PEG-CDs by MCF-7/ADR cells was concentration- and time-dependent (Figures 6A and B), which was consistent with other particles^{11, 41}. RGD modification could apparently increase the cellular uptake compared to PEG-CDs, owing to the highly expressed $\alpha_v\beta_3$ on tumor cells such as MCF-7/ADR cells²⁹, which was the specific receptor of RGD⁴². These results demonstrated RGD-PEG-CDs could target to MCF-7/ADR cells, thus they might be used for breast tumor imaging. Additionally, the expression of P-gp on MCF-7/ADR cells lead to the cells hard to be killed by chemotherapeutics⁴³. In this study, it was showed MCF-7/ADR cells could obviously uptake of RGD-PEG-CDs with high intensity, suggesting the RGD-PEG-CDs could be served as carriers to deliver chemotherapeutics into MCF-7/ADR cells to conquer the drug resistance.

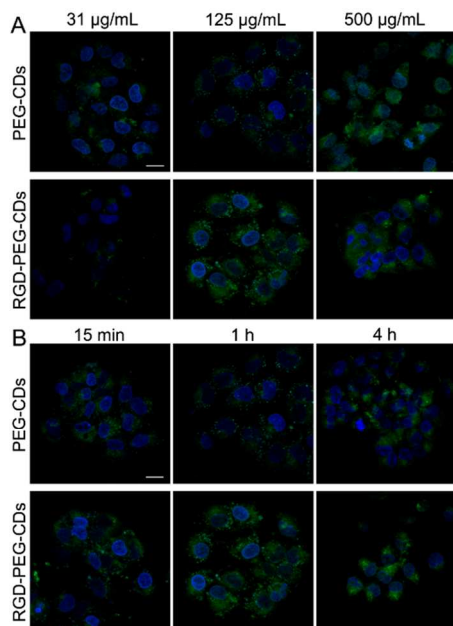


Figure 6. Cellular uptake of PEG-CDs and RGD-PEG-CDs by MCF-7/ADR cells. A: Concentration related uptake by MCF-7/ADR cells after 1 h incubation, bar represents 10 μm . B: Time related uptake by MCF-7/ADR cells after incubation with 125 $\mu\text{g/mL}$ of PEG-CDs and RGD-PEG-CDs, bar represents 20 μm .

Uptake mechanism

To determine the uptake pathways that involved in the uptake procedure of PEG-CDs and RGD-PEG-CDs, various inhibitors were used. Obviously, the uptake of both PEG-CDs and RGD-PEG-CDs by MCF-7/ADR cells was energy-dependent, because the uptake was significantly reduced to 39.3% and 46.1% respectively after energy depletion by sodium azide and to 41.3% and 31.1% respectively after incubation at 4 $^{\circ}\text{C}$ (Figure 7). Colchicine and nocodazole, the inhibitors of macropinocytosis, significantly decreased the cellular uptake of PEG-CDs to 31.2% and 40.6% respectively and decreased the cellular uptake of RGD-PEG-CDs to 33.1% and 38.9% respectively, suggesting that macropinocytosis was involved in the uptake of both PEG-CDs and RGD-PEG-CDs. Filipin, a special inhibitor of caveolae-mediated endocytosis⁴⁴, significantly decreased the uptake of PEG-CDs and RGD-PEG-CDs to 59.5% and 60.7% respectively, suggesting caveolae-mediated endocytosis was also considerably involved in the uptake procedure. The positive charge inhibitor PLL⁴⁵, could only inhibited the uptake of PEG-CDs and RGD-CDs to approximately 70.3% and 67.0% respectively, indicating the internalization of these two particles were not mediated by charge interaction. Additionally, free RGD significantly inhibited the uptake of RGD-PEG-CDs to 41.8%, while RGD could not considerably inhibit the uptake of PEG-CDs, suggesting the internalization of RGD-PEG-CDs was mediated by specific receptor of RGD, which was consistent with previous studies⁴⁶.

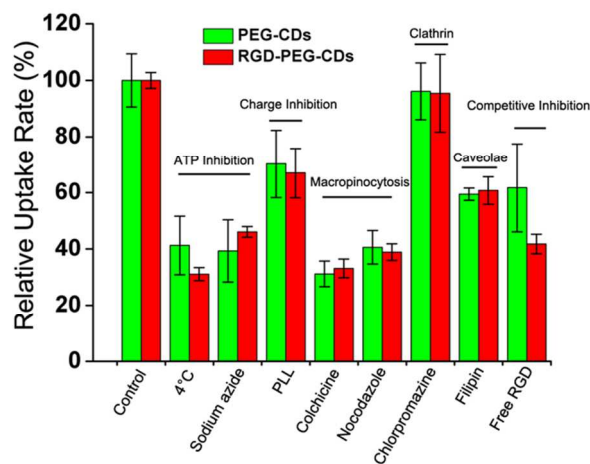


Figure 7. MCF-7/ADR uptake of PEG-CDs and RGD-CDs at the presence of various inhibitors.

In vivo and ex vivo imaging

In vivo imaging is one of the most common and powerful non-invasive diagnosis methods. After intravenous injection of PEG-CDs and RGD-PEG-CDs, obvious fluorescent distribution could be observed in the whole body especially in the liver (Figure 8A), because the liver is the main organ to eliminate foreign materials from the blood circulation. However, the distribution in MCF-7/ADR xenografts was different between PEG-CDs and RGD-PEG-CDs. The highest distribution of PEG-CDs in tumor was observed at 30 min after intravenous injection, and then the fluorescent intensity gradually decreased during the time expanding, which was contributed to EPR effect¹⁹. Comparatively, the distribution of RGD-PEG-CDs in tumor was much higher than that of PEG-CDs at almost all time points, suggesting functionalization with RGD could improve the tumor targeting efficiency of PEG-CDs, contributing to the targeting effect of RGD that mediated by highly expressed $\alpha_v\beta_3$ on tumor⁴⁷, which was consistent with in vitro cellular uptake results. Ex vivo imaging of various tissues further demonstrated the distribution of RGD-PEG-CDs was much higher than that of PEG-CDs (Figure 8B), and the former was approximately 1.7-fold higher than the latter (Figure 8C). However, the distribution of RGD-PEG-CDs in lung and kidney was also higher than that of PEG-CDs (Figures 8B and C). These results demonstrated that nanoscale CDs with PEG modification possess photoluminescence property, which was due to the quantum confinement effect⁴⁸. After modification with PEG, it could reduce the adsorption by plasma proteins and significantly improve the cycle time. However, it is insufficient to deliver the CDs to tumor site after conjugation with PEG. To further improve the delivery and target efficiency, it is necessary to conjugate PEG-CDs with specific ligand. Thus, RGD, a specific ligand targeted to integrin receptor was conjugated to the PEG-CDs, which could significantly deliver the CDs to tumor site and improve bio-imaging efficiency²⁵. In addition, the relative long excitation and emission wavelength was also important for the application of CDs on bio-imaging².

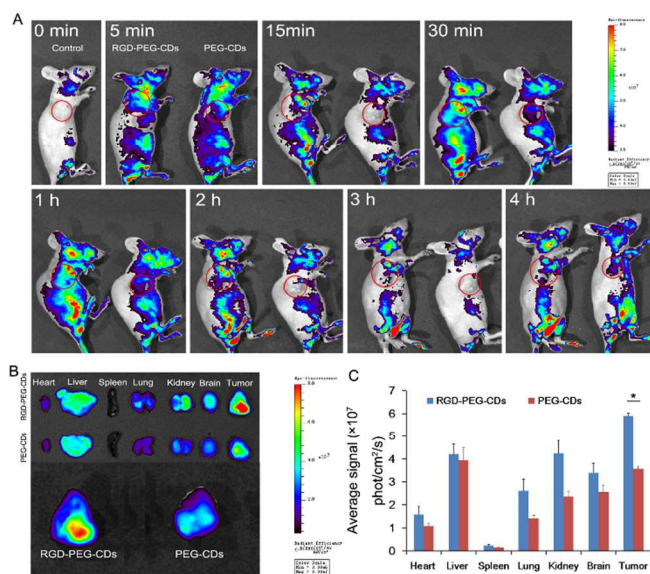


Figure 8. In vivo and ex vivo imaging of PEG-CDs and RGD-PEG-CDs treated MCF-7/ADR xenografts bearing mice. A: In vivo imaging of MCF-7/ADR xenografts bearing mice at different times after injected with PEG-CDs and RGD-PEG-CDs. B: Ex vivo imaging of tissues at 4 h after injected with PEG-CDs and RGD-PEG-CDs. C: Semi-quantitative fluorescent intensity of different kinds of organs. * $p < 0.05$.

Tissue distribution

Microvessels were stained using anti-CD31 antibody to elucidate the targeting ability of RGD-PEG-CDs. The distribution of PEG-CDs in tumor was relative low and showed poor colocalization with microvessel (Figure 9). In contrast, the RGD-PEG-CDs showed well colocalization with microvessel, suggesting RGD-PEG-CDs could target the microvessel, which overexpressed $\alpha_v\beta_3$. Thus RGD-PEG-CDs could be used for delivering anti-angiogenesis drugs to the endothelial cells of microvessel, resulting in disrupting of blood supply to tumor.

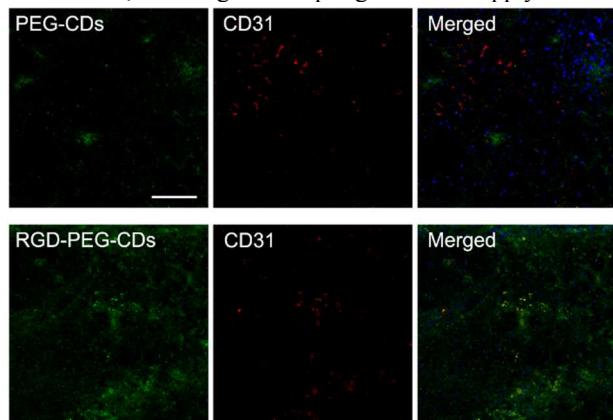


Figure 9. Distribution of PEG-CDs and RGD-PEG-CDs in tumor slices. neovessels were stained by anti-CD31 antibody. Blue represents nuclei which stained by DAPI and bar represents 100 μm .

The distribution in slices of normal tissues were similar to the results of ex vivo imaging (Figure 10). In most tissues, there was no obvious difference between PEG-CDs and RGD-PEG-CDs. But in kidney, the distribution of RGD-PEG-CDs was higher than that of PEG-CDs, which was consistent with previous studies that showed higher accumulation in kidney of RGD modified probes⁴⁹. Additionally, the modification of

RGD also could elevate the distribution in brain, which was due to the expression of $\alpha_v\beta_3$ on brain endothelial cells⁴⁶.

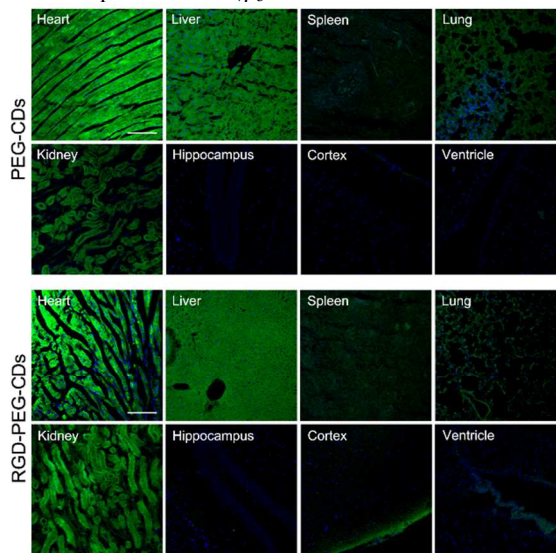


Figure 10. Distribution of PEG-CDs and An-PEG-CDs in normal tissue slices. Bar represents 100 μm .

Conclusion

In this study, a kind of CDs was prepared with long excitation/emission wavelength. After surface modification, RGD-PEG-CDs possessed well plasma stability, well hemocompatibility and low cytotoxicity. In vitro, RGD-PEG-CDs could be taken up by MCF-7/ADR cells at a density higher than PEG-CDs through a time-, concentration- and energy-dependent manner. The uptake of RGD-PEG-CDs was involved in endosomes, mainly contributing to macropinocytosis and caveolae mediated pathway. In vivo, RGD-PEG-CDs could target to MCF-7/ADR xenografts, which was significantly better than PEG-CDs. Fluorescent distribution in tumor slices further demonstrated the RGD-PEG-CDs could target to microvessel, owing to the highly expressed $\alpha_v\beta_3$ on microvessel. These results demonstrated RGD-PEG-CDs were a promising probe for MCF-7/ADR tumor imaging.

Acknowledgements

The work was granted by National Natural Science Foundation of China (81402866, 81301974) and the Sichuan University Starting Foundation for Young Teachers (2014SCU11044).

Notes and references

^aKey Laboratory of Drug Targeting and Drug Delivery Systems, West China School of Pharmacy, Sichuan University, No. 17, Block 3, Southern Renmin Road, Chengdu, 610041, China.

^bKey Laboratory of Smart Drug Delivery (Fudan University), Ministry of Education; School of Pharmacy, Fudan University; 826 Zhangheng Road, Shanghai, 201203, China.

¹ Contributed equally to this work.

* Corresponding author: Gao H.: Fax: 86 28 85502532; Tel: 86 28 85502575; E-mail: gaohuile@scu.edu.cn; He Q.: qinhe@scu.edu.cn

1. K. I. Joo, Y. Fang, Y. Liu, L. Xiao, Z. Gu, A. Tai, C. L. Lee, Y. Tang and P. Wang, Enhanced real-time monitoring of adeno-associated

- virus trafficking by virus-quantum dot conjugates, *ACS Nano*, 2011, 5, 3523-3535.
- J. Li and J. J. Zhu, Quantum dots for fluorescent biosensing and bio-imaging applications, *Analyst*, 2013, 138, 2506-2515.
 - Du F, Y. Ming, F. Zeng, C. Yu and S. Wu, A low cytotoxic and ratiometric fluorescent nanosensor based on carbon-dots for intracellular pH sensing and mapping, *Nanotechnology*, 2013, 24, 365101.
 - H. Li, Z. Kang, Y. Liu and S. Lee, Carbon nanodots: synthesis, properties and applications, *J Mater Chem*, 2012, 22, 24230-24253.
 - S. N. Baker and G. A. Baker, Luminescent carbon nanodots: emergent nanolights, *Angew Chem Int Ed Engl*, 2010, 49, 6726-6744.
 - L. Cao, X. Wang, M. J. Mezziani, F. Lu, H. Wang, P. G. Luo, Y. Lin, B. A. Harruff, L. M. Veca, D. Murray, S. Y. Xie and Y. P. Sun, Carbon dots for multiphoton bioimaging, *J Am Chem Soc*, 2007, 129, 11318-11319.
 - B. Chen, F. Li, S. Li, W. Weng, H. Guo, T. Guo, X. Zhang, Y. Chen, T. Huang, X. Hong, S. You, Y. Lin, K. Zeng and S. Chen, Large scale synthesis of photoluminescent carbon nanodots and their application for bioimaging, *Nanoscale*, 2013, 5, 1967-1971.
 - S. Sahu, B. Behera, T. K. Maiti and S. Mohapatra, Simple one-step synthesis of highly luminescent carbon dots from orange juice: application as excellent bio-imaging agents, *Chem Commun (Camb)*, 2012, 48, 8835-8837.
 - S. Liu, J. Tian, L. Wang, Y. Luo, J. Zhai and X. Sun, Preparation of photoluminescent carbon nitride dots from CCl₄ and 1,2-ethylenediamine: a heat-treatment-based strategy, *J Mater Chem*, 2011, 21, 11726-11729.
 - S. K. Bhunia, A. Saha, A. R. Maity, S. C. Ray and N. R. Jana, Carbon Nanoparticle-based Fluorescent Bioimaging Probes, *Sci Rep*, 2013, 3, 1473.
 - S. Ruan, B. Zhu, H. Zhang, J. Chen, S. Shen, J. Qian, Q. He and H. Gao, A simple one-step method for preparation of fluorescent carbon nanospheres and the potential application in cell organelles imaging, *J Colloid Interface Sci*, 2014, 422, 25-29.
 - H. Y. Ko, Y. W. Chang, G. Paramasivam, M. S. Jeong, S. Cho and S. Kim, In vivo imaging of tumour bearing near-infrared fluorescence-emitting carbon nanodots derived from tire soot, *Chem Commun (Camb)*, 2013, 49, 10290-10292.
 - S. Zhu, Q. Meng, L. Wang, J. Zhang, Y. Song, H. Jin, K. Zhang, H. Sun, H. Wang and B. Yang, Highly photoluminescent carbon dots for multicolor patterning, sensors, and bioimaging, *Angew Chem Int Ed Engl*, 2013, 52, 3953-3957.
 - Y. Shi, L. Liu, H. Pang, H. Zhou, G. Zhang, Y. Ou, X. Zhang, Du J and W. Xiao, Facile preparation of highly luminescent CdTe quantum dots within hyperbranched poly(amidoamine)s and their application in bio-imaging, *Nanoscale Res Lett*, 2014, 9, 115.
 - S. Ruan, J. Qian, S. Shen, J. Chen, J. Zhu, X. Jiang, Q. He, W. Yang and H. Gao, Fluorescent carbonaceous nanodots for noninvasive glioma imaging after angiopep-2 decoration, *Bioconjug Chem*, 2014, 25, 2252-2259.
 - S. Ruan, J. Wan, Y. Fu, K. Han, X. Li, J. Chen, Q. Zhang, S. Shen, Q. He and H. Gao, PEGylated Fluorescent Carbon Nanoparticles for Noninvasive Heart Imaging, *Bioconjug Chem*, 2014, 25, 1061-1068.
 - K. Kawano, M. Watanabe, T. Yamamoto, M. Yokoyama, P. Opanasopit, T. Okano and Y. Maitani, Enhanced antitumor effect of camptothecin loaded in long-circulating polymeric micelles, *J Control Release*, 2006, 112, 329-332.
 - M. Zhou, X. Zhang, Y. Yang, Z. Liu, B. Tian, J. Jie and X. Zhang, Carrier-free functionalized multidrug nanorods for synergistic cancer therapy, *Biomaterials*, 2013, 34, 8960-8967.
 - F. Yuan, M. Dellian, D. Fukumura, M. Leunig, D. A. Berk, V. P. Torchilin and R. K. Jain, Vascular permeability in a human tumor xenograft: molecular size dependence and cutoff size, *Cancer Res*, 1995, 55, 3752-3756.
 - J. Fang, H. Nakamura and H. Maeda, The EPR effect: Unique features of tumor blood vessels for drug delivery, factors involved, and limitations and augmentation of the effect, *Adv Drug Deliv Rev*, 2011, 63, 136-151.
 - H. Xiao, R. Qi, S. Liu, X. Hu, T. Duan, Y. Zheng, Y. Huang and X. Jing, Biodegradable polymer - cisplatin(IV) conjugate as a pro-drug of cisplatin(II), *Biomaterials*, 2011, 32, 7732-7739.
 - Y. Liu, J. Fang, K. I. Joo, M. K. Wong and P. Wang, Codelivery of chemotherapeutics via crosslinked multilamellar liposomal vesicles to overcome multidrug resistance in tumor, *PLoS One*, 2014, 9, e110611.
 - Y. Liu, J. Fang, Y. J. Kim, M. K. Wong and P. Wang, Codelivery of doxorubicin and paclitaxel by cross-linked multilamellar liposome enables synergistic antitumor activity, *Mol Pharm*, 2014, 11, 1651-1661.
 - C. H. Choi, C. A. Alabi, P. Webster and M. E. Davis, Mechanism of active targeting in solid tumors with transferrin-containing gold nanoparticles, *Proc Natl Acad Sci U S A*, 2010, 107, 1235-1240.
 - H. Gao, Z. Yang, S. Zhang, S. Cao, S. Shen, Z. Pang and X. Jiang, Ligand modified nanoparticles increases cell uptake, alters endocytosis and elevates glioma distribution and internalization, *Sci Rep*, 2013, 3, 2534.
 - Abdullah-Al-Nahain, J. E. Lee, I. In, H. Lee, K. D. Lee, J. H. Jeong and S. Y. Park, Target delivery and cell imaging using hyaluronic acid-functionalized graphene quantum dots, *Mol Pharm*, 2013, 10, 3736-3744.
 - X. Chen, Y. Tang, B. Cai and H. Fan, 'One-pot' synthesis of multifunctional GSH-CdTe quantum dots for targeted drug delivery, *Nanotechnology*, 2014, 25, 235101.
 - M. Schottelius, B. Laufer, H. Kessler and H. J. Wester, Ligands for mapping alphavbeta3-integrin expression in vivo, *Acc Chem Res*, 2009, 42, 969-980.
 - L. Vellon, J. A. Menendez, H. Liu and R. Lupu, Up-regulation of alphavbeta3 integrin expression is a novel molecular response to chemotherapy-induced cell damage in a heregulin-dependent manner, *Differentiation*, 2007, 75, 819-830.
 - E. Ruoslahti, RGD and other recognition sequences for integrins, *Annu Rev Cell Dev Biol*, 1996, 12, 697-715.
 - R. Haubner, H. J. Wester, F. Burkhart, R. Senekowitsch-Schmidtke, W. Weber, S. L. Goodman, H. Kessler and M. Schwaiger, Glycosylated RGD-containing peptides: tracer for tumor targeting and angiogenesis imaging with improved biokinetics, *J Nucl Med*, 2001, 42, 326-336.
 - W. Wei, X. He and N. Ma, DNA-templated assembly of a heterobivalent quantum dot nanoprobe for extra- and intracellular

- dual-targeting and imaging of live cancer cells, *Angew Chem Int Ed Engl*, 2014, 53, 5573-5577.
33. J. Qian, J. Chen, S. Ruan, S. Shen, Q. He, X. Jiang, J. Zhu and H. Gao, Preparation and biological evaluation of photoluminescent carbonaceous nanospheres, *J Colloid Interface Sci*, 2014, 429, 77-82.
34. H. Gao, S. Cao, C. Chen, S. Cao, Z. Yang, Z. Pang, Z. Xi, S. Pan, Q. Zhang and X. Jiang, Incorporation of lapatinib into lipoprotein-like nanoparticles with enhanced water solubility and anti-tumor effect in breast cancer, *Nanomedicine (Lond)*, 2013, 8, 1429-1442.
35. H. Gao, S. Pan, Z. Yang, S. Cao, C. Chen, X. Jiang, S. Shen, Z. Pang and Y. Hu, A cascade targeting strategy for brain neuroglial cells employing nanoparticles modified with angioprep-2 peptide and EGFP-EGF1 protein, *Biomaterials*, 2011, 32, 8669-8675.
36. W. Li, Z. Zhang, B. Kong, S. Feng, J. Wang, L. Wang, J. Yang, F. Zhang, P. Wu and D. Zhao, Simple and green synthesis of nitrogen-doped photoluminescent carbonaceous nanospheres for bioimaging, *Angew Chem Int Ed Engl*, 2013, 52, 8151-8155.
37. J. Qian, S. Ruan, X. Cao, X. Cun, J. Chen, S. Shen, X. Jiang, Q. He, J. Zhu and H. Gao, Fluorescent carbonaceous nanospheres as biological probe for noninvasive brain imaging, *J Colloid Interface Sci*, 2014, 436C, 227-233.
38. M. Sevilla and A. B. Fuertes, Chemical and Structural Properties of Carbonaceous Products Obtained by Hydrothermal Carbonization of Saccharides, *Chemistry - A European Journal*, 2009, 15, 4195-4203.
39. S. Liu, J. Tian, L. Wang, Y. Zhang, X. Qin, Y. Luo, A. M. Asiri, A. O. Al-Youbi and X. Sun, Hydrothermal Treatment of Grass: A Low-Cost, Green Route to Nitrogen-Doped, Carbon-Rich, Photoluminescent Polymer Nanodots as an Effective Fluorescent Sensing Platform for Label-Free Detection of Cu(II) Ions, *Adv Mater*, 2012, 24, 2037-2041.
40. H. Gao and Q. He, The interaction of nanoparticles with plasma proteins and the consequent influence on nanoparticles behavior, *Expert Opin Drug Deliv*, 2014, 11, 409-420.
41. H. Gao, G. Hu, Q. Zhang, S. Zhang, X. Jiang and Q. He, Pretreatment with chemotherapeutics for enhanced nanoparticles accumulation in tumor: the potential role of G2 cycle retention effect, *Sci Rep*, 2014, 4, 4492.
42. E. Ruoslahti and M. D. Pierschbacher, New perspectives in cell adhesion: RGD and integrins, *Science*, 1987, 238, 491-497.
43. D. Xu, Q. Lu and X. Hu, Down-regulation of P-glycoprotein expression in MDR breast cancer cell MCF-7/ADR by honokiol, *Cancer Lett*, 2006, 243, 274-280.
44. C. Lamaze and S. L. Schmid, The emergence of clathrin-independent pinocytic pathways, *Curr Opin Cell Biol*, 1995, 7, 573-580.
45. Q. Zhang, J. Tang, L. Fu, R. Ran, Y. Liu, M. Yuan and Q. He, A pH-responsive alpha-helical cell penetrating peptide-mediated liposomal delivery system, *Biomaterials*, 2013, 34, 7980-7993.
46. Y. Liu, R. Ran, J. Chen, Q. Kuang, J. Tang, L. Mei, Q. Zhang, H. Gao, Z. Zhang and Q. He, Paclitaxel loaded liposomes decorated with a multifunctional tandem peptide for glioma targeting, *Biomaterials*, 2014, 35, 4835-4847.
47. S. Chatterjee, A. Matsumura, J. Schradermeier and G. Y. Gillespie, Human malignant glioma therapy using anti-alpha(v)beta3 integrin agents, *J Neurooncol*, 2000, 46, 135-144.
48. L. P. McGuinness, Y. Yan, A. Stacey, D. A. Simpson, L. T. Hall, D. Maclaurin, S. Prawer, P. Mulvaney, J. Wrachtrup, F. Caruso, R. E. Scholten and L. C. Hollenberg, Quantum measurement and orientation tracking of fluorescent nanodiamonds inside living cells, *Nat Nanotechnol*, 2011, 6, 358-363.
49. K. H. Jung, K. H. Lee, J. Y. Paik, B. H. Ko, J. S. Bae, B. C. Lee, H. J. Sung, D. H. Kim, Y. S. Choe and D. Y. Chi, Favorable biokinetic and tumor-targeting properties of ^{99m}Tc-labeled glucosamine RGD and effect of paclitaxel therapy, *J Nucl Med*, 2006, 47, 2000-2007.

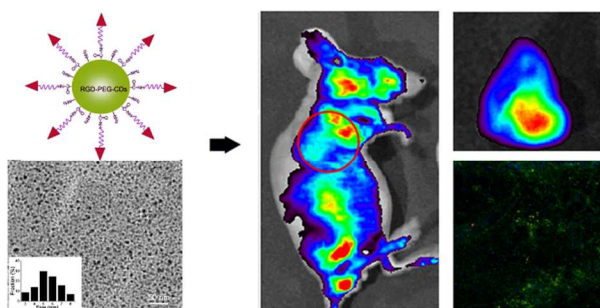


Table of content

RGD functionalized carbonaceous dots were prepared and utilized for non-invasive breast cancer imaging.